

BIRTH OF THE GALACTIC DISK REVEALED BY THE H3 SURVEY

CHARLIE CONROY¹, DAVID H. WEINBERG², ROHAN P. NAIDU^{3,4}, TOBIAS BUCK^{5,6}, JAMES W. JOHNSON⁷, PHILLIP CARGILE¹, ANA BONACA⁷, NELSON CALDWELL¹, VEDANT CHANDRA¹, JIWON JESSE HAN¹, BENJAMIN D. JOHNSON¹, JOSHUA S. SPEAGLE^{8,9,10,11}, YUAN-SEN TING^{2,12,13}, TURNER WOODY¹, DENNIS ZARITSKY¹⁴

Version July 24, 2024

ABSTRACT

We use chemistry ($[\alpha/\text{Fe}]$ and $[\text{Fe}/\text{H}]$), main sequence turnoff ages, and kinematics determined from H3 Survey spectroscopy and *Gaia* astrometry to identify the birth of the Galactic disk. We separate in-situ and accreted stars on the basis of angular momenta and eccentricities. The sequence of high- α in-situ stars persists down to at least $[\text{Fe}/\text{H}] \approx -2.5$ and shows unexpected non-monotonic behavior: with increasing metallicity the population first declines in $[\alpha/\text{Fe}]$, then increases over the range $-1.3 \lesssim [\text{Fe}/\text{H}] \lesssim -0.7$, and then declines again at higher metallicities. The number of stars in the in-situ population rapidly increases above $[\text{Fe}/\text{H}] \approx -1$. The average kinematics of these stars are hot and independent of metallicity at $[\text{Fe}/\text{H}] \lesssim -1$ and then become increasingly cold and disk-like at higher metallicities. The ages of the in-situ, high- α stars are uniformly very old (≈ 13 Gyr) at $[\text{Fe}/\text{H}] \lesssim -1.3$, and span a wider range (8–12 Gyr) at higher metallicities. Interpreting the chemistry with a chemical evolution model suggests that the non-monotonic behavior is due to a significant increase in star formation efficiency, which began ≈ 13 Gyr ago. These results support a picture in which the first ≈ 1 Gyr of the Galaxy was characterized by a “simmering phase” in which the star formation efficiency was low and the kinematics had substantial disorder with some net rotation. The disk then underwent a dramatic transformation to a “boiling phase”, in which the star formation efficiency increased substantially, the kinematics became disk-like, and the number of stars formed increased tenfold. We interpret this transformation as the birth of the Galactic disk at $z \approx 4$. The physical origin of this transformation is unclear and does not seem to be reproduced in current galaxy formation models.

1. INTRODUCTION

A thorough understanding of the components of the Galaxy, including their formation channel(s) and dynamical evolution, is of great interest for several reasons. As the best-studied galaxy in the universe, the Milky Way provides stringent tests of galaxy formation models (e.g., Guedes et al. 2011; Wetzel et al. 2016; Grand et al. 2017; Buck et al. 2021). The kinematics of stars in the Galaxy can be very precisely measured, and therefore may offer novel constraints on the nature dark matter (e.g., Ibata et al. 2002; Johnston et al. 2002; Bovy et al.

2017; Bonaca et al. 2019). There is also a basic and deep human desire to understand our origins, from the smallest scales to the Galactic ecosystem.

The rotationally-supported disk contains the majority of the stars in the Galaxy. It has long been known that the disk harbors multiple components (or populations) in the space of chemistry, kinematics, spatial extent, and age (e.g., Gilmore & Reid 1983; Norris et al. 1985; Chiba & Beers 2000; Nissen & Schuster 2010; Bovy et al. 2012; Haywood et al. 2013; Hayden et al. 2015); see Rix & Bovy (2013) and Bland-Hawthorn & Gerhard (2016) for recent reviews. Spatially, there is evidence for thin and thick disks with different scale heights. Chemically, a clear dichotomy exists in the abundance of α elements relative to iron ($[\alpha/\text{Fe}]$) – a high- α and a low- α population. In general, the former has older ages and a larger scale-height than the latter. While the correspondence between high- α and thick disk and low- α and thin disk is reasonably strong in the solar vicinity, this correspondence breaks down especially strongly at larger galactocentric distances (e.g., Hayden et al. 2015).

The origin of these two disk populations has been the subject of much debate. One scenario envisions the chemical dichotomy as the result of smooth evolution of the Galaxy in terms of its star formation rate (SFR), gas mass, etc., combined with radial mixing, kinematic heating, or a decline in the vertical dispersion of the gas with time to explain the observed correlations between kinematics, chemistry, and scale-height (e.g., Schönrich & Binney 2009; Loebman et al. 2011; Bird et al. 2013; Minchev et al. 2015; Sharma et al. 2021). A second scenario invokes a violent event such as a merger as the origin of the dichotomy (e.g., Reddy et al. 2006; Villalobos & Helmi 2008; Grand et al. 2018a; Mackereth et al. 2018; Bonaca et al. 2020; Buck 2020; Agertz et al. 2021).

¹ Center for Astrophysics | Harvard & Smithsonian, Cambridge, MA, 02138, USA

² Department of Astronomy & CCAPP, The Ohio State University, 140 W. 18th Avenue Columbus, OH 43210, USA

³ NASA Hubble Fellow

⁴ MIT Kavli Institute for Astrophysics and Space Research, 77 Massachusetts Ave., Cambridge, MA 02139, USA

⁵ Interdisziplinäres Zentrum für Wissenschaftliches Rechnen, Universität Heidelberg, Im Neuenheimer Feld 205, D-69120 Heidelberg, Germany

⁶ Zentrum für Astronomie, Institut für Theoretische Astrophysik, Universität Heidelberg, Albert-Ueberle-Strasse 2, D-69120 Heidelberg, Germany

⁷ The Observatories of the Carnegie Institution for Science, 813 Santa Barbara St., Pasadena, CA 91101, USA

⁸ Banting & Dunlap Fellow

⁹ Department of Statistical Sciences, University of Toronto, Toronto, ON M5S 3G3, Canada

¹⁰ David A. Dunlap Department of Astronomy & Astrophysics, University of Toronto, Toronto, ON M5S 3H4, Canada

¹¹ Dunlap Institute for Astronomy & Astrophysics, University of Toronto, Toronto, ON M5S 3H4, Canada

¹² Research School of Astronomy & Astrophysics, Australian National University, Cotter Road, Weston Creek, ACT 2611, Canberra, Australia

¹³ Research School of Computer Science, Australian National University, Acton ACT 2601, Australia

¹⁴ Steward Observatory, University of Arizona, 933 North Cherry Avenue, Tucson, AZ 85721, USA

In this picture the high- α disk forms first and is truncated at $z \sim 1$ by a merger that heats the existing disk stars and delivers fresh gas to fuel the formation of the low- α disk. A related idea is the two-infall model (Chiappini et al. 1997; Spitoni et al. 2019), which posits two time-separated phases of accretion with an intervening lull of star formation. This model is agnostic regarding the origin of the two-phase accretion history. A third scenario suggests that most or all of the thick disk was formed directly from the accretion of disrupting satellite galaxies on prograde orbits (Abadi et al. 2003).

Thanks to the combination of *Gaia* astrometry and large spectroscopic surveys, our understanding of stars on halo-like orbits has improved dramatically over the past several years. One striking discovery was the identification of stars with chemistry indistinguishable from the high- α disk with halo-like orbits (e.g., Bonaca et al. 2017; Haywood et al. 2018; Di Matteo et al. 2019; Belokurov et al. 2020b; Bonaca et al. 2020). One interpretation of this population is that the stars were born in-situ and subsequently dynamically heated to halo-like orbits, a phenomenon predicted by some simulations (e.g., Zolotov et al. 2009). The age distribution of these “in-situ halo” stars is truncated at lookback times of 8–11 Gyr (Gallart et al. 2019; Bonaca et al. 2020; Belokurov et al. 2020b; Xiang & Rix 2022), suggesting that the heating event, perhaps a merger, occurred at $z \sim 1-2$ (see also Vincenzo et al. 2019; Chaplin et al. 2020; Montalbán et al. 2021).

A large number of accreted systems have also been identified as comprising the accreted stellar halo (e.g., Belokurov et al. 2018; Helmi et al. 2018; Koppelman et al. 2018; Myeong et al. 2019; Naidu et al. 2020; Horta et al. 2021). By far the most significant is the *Gaia*-Sausage Enceladus (GSE) system, which comprises most of the accreted halo within 30 kpc of the Galactic center. Naidu et al. (2021) combined a suite of N -body simulations and kinematic and age data from the H3 Survey (Conroy et al. 2019) to argue that the GSE merger completed approximately 8 Gyr ago, and gave rise to the in-situ halo by heating pre-existing disk stars. There is circumstantial evidence for another major accretion event in the inner Galaxy, perhaps as massive as GSE (e.g., Kruijssen et al. 2019; Massari et al. 2019; Horta et al. 2021; Naidu et al. 2022). It is possible that there are not one but several accreted structures in the inner Galaxy. In any event, it is likely that the accreted stars in the inner Galaxy were brought in from a merger that occurred prior to GSE, i.e., at $z > 1$.

While the characterization and origins of the main disk and halo populations are coming into focus, the very earliest epochs of the Galaxy and the emergence of the disk are still poorly understood. Stellar metallicity is often invoked as a proxy for age, and so studying the most metal poor stars may offer clues to early epochs. Stars associated with a disk component of our Galaxy have indeed been found at low metallicities (e.g., Norris et al. 1985; Morrison et al. 1990; Chiba & Beers 2000; Carollo et al. 2019; Naidu et al. 2020). This population, sometimes known as the metal-weak thick disk, has been identified at metallicities as low as $[\text{Fe}/\text{H}] = -2.5$, and generally has hotter kinematics than the canonical thick disk at higher metallicity (Carollo et al. 2019). Recently, several authors have identified very metal-poor stars ($[\text{Fe}/\text{H}] < -2.5$) with low eccentricities reminiscent of the thin disk (Sestito et al. 2020; Carter et al. 2021). Using $[\text{Al}/\text{Fe}]$ from APOGEE (Majewski et al. 2017) to separate in-situ from accreted stars, Belokurov & Kravtsov (2022) identified in-situ stars to $[\text{Fe}/\text{H}] \approx -1.5$. The average tangential velocity of the in-situ stars in their sample increased rapidly at $[\text{Fe}/\text{H}] \approx -1$. They identify

this transition as the epoch when the Galaxy spun up from a relatively disordered state to well-ordered rotation.

In this paper we use H3 spectroscopy and *Gaia* astrometry to identify and characterize in-situ stars from $-2.5 \lesssim [\text{Fe}/\text{H}] \lesssim 0.5$. We chart the chemistry in terms of the abundance ratio $[\alpha/\text{Fe}]$, and we report main sequence turnoff and subgiant ages and average kinematic behavior as a function of metallicity. These measurements allow us to identify the birth of the Galactic disk associated with a major transformation in the disk that began ≈ 13 Gyr ago when the mean metallicity was $[\text{Fe}/\text{H}] \approx -1.3$.

2. DATA

In this paper we use data from the H3 Stellar Spectroscopic Survey (Conroy et al. 2019) and *Gaia* EDR3 (*Gaia* Collaboration et al. 2021). H3 is collecting $R = 32,000$ spectra over the wavelength range $5150\text{\AA} - 5300\text{\AA}$ using the Hectochelle spectrograph on the MMT telescope (Fabricant et al. 2005; Szentgyorgyi et al. 2011). The survey will eventually collect 300,000 spectra over ≈ 1500 uniformly spaced fields covering $|b| > 20^\circ$ and $\text{Dec.} > -20^\circ$. As of March 2022 the survey has collected 208,000 spectra over 1,100 fields. The primary survey selection function is based solely on magnitude ($15 < r < 18$) and *Gaia* parallax (a selection that has evolved from $\pi < 0.5$ mas to $\pi < 0.3$ mas as the *Gaia* data quality has improved). The survey includes additional rare high-value targets and filler targets that are both fainter and at higher parallax than the main sample. The high parallax filler sample constitutes $\approx 60\%$ of the sample used below.

Stellar parameters are derived using the MINESweeper program (Cargile et al. 2020). MINESweeper simultaneously fits the high-resolution spectrum and the broadband photometry (from SDSS, Pan-STARRS, *Gaia*, 2MASS, *WISE*) to a library of synthetic spectral grids and isochrones. Derived parameters include radial velocities, distances, reddening, rotational line broadening, V_{rot} , $[\text{Fe}/\text{H}]$, and $[\alpha/\text{Fe}]$. In the model fitting we assume that O, Ne, Mg, Si, Ar, Ca, and Ti vary in lock-step and we refer to them as α elements. The fitted spectral region contains the Mg I triplet as well as many Fe I and Fe II lines, so $[\alpha/\text{Fe}]$ is primarily determined by Mg and Fe lines. MINESweeper employs a Bayesian framework and includes the *Gaia* parallax as a prior on the distance. The standard pipeline includes a complex prior on the stellar age (see Cargile et al. 2020, for details). Here, since we are particularly interested in ages, we use an alternative version of the pipeline in which the age prior is flat from 4–14 Gyr. We have also tested the effect of the isochrones on the abundances by fitting the spectra to a version of MINESweeper in which the spectroscopic parameters are determined without the requirement that the star reside on an isochrone. For the sample discussed below, the differences are small and within the reported uncertainties ($\approx 0.01 - 0.02$) for $[\text{Fe}/\text{H}]$ and $[\alpha/\text{Fe}]$.

The MIST isochrones (Choi et al. 2016), which we use in this work, include the effects of diffusion on the surface abundances (specifically, we use MIST v2.1 isochrones, which include several improvements and extension to $[\alpha/\text{Fe}]$ variation; see Dotter et al. in prep for details). This effect is largest around the main sequence turnoff (Dotter et al. 2017), where much of our sample is located. MINESweeper adopts the initial metallicity and composition as the free variables, but the surface abundance is used when comparing to the data. The program therefore returns both the surface and the initial abundances. The latter are used in this work as they are more fundamental and should exhibit less variation than sur-

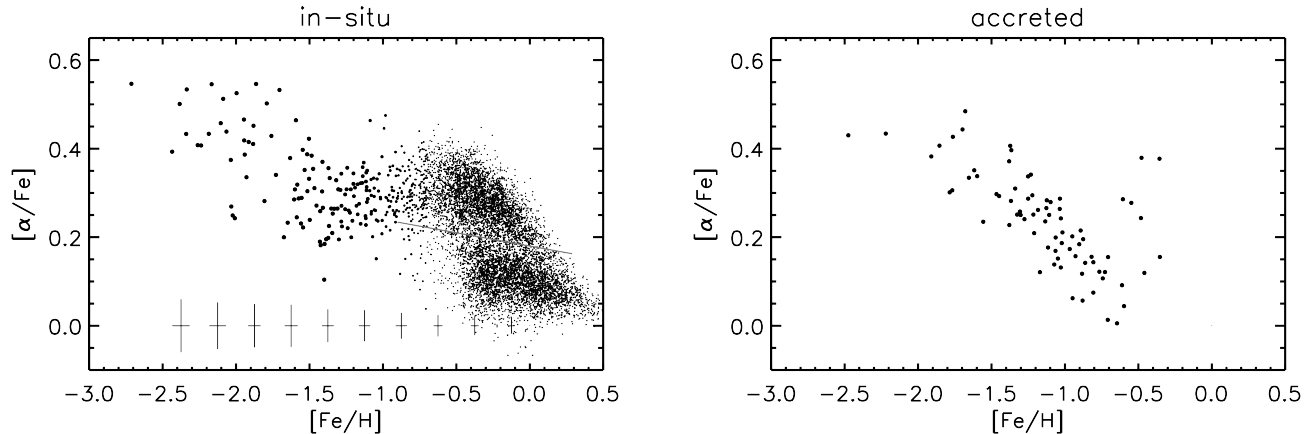


Figure 1. Chemistry of in-situ and accreted stars from the H3 Survey. In-situ stars are defined to have prograde orbits ($L_Z < 0$) with eccentricities $e < 0.8$, while accreted stars are defined to have $e > 0.9$ or a combination of $e > 0.8$ and $L_Z > 500 \text{ km s}^{-1} \text{ kpc}^{-1}$ (retrograde orbits). In the left panel, one clearly sees the high- α and low- α sequences at $[\text{Fe}/\text{H}] \gtrsim -0.7$. Moving to lower metallicities the high- α population declines in $[\alpha/\text{Fe}]$ until $[\text{Fe}/\text{H}] \approx -1.3$, at which point $[\alpha/\text{Fe}]$ increases. The grey line highlights our adopted separation between high- α and low- α populations. The accreted population (right panel) displays a linear decline in $[\alpha/\text{Fe}]$ with increasing metallicity. The ≈ 7 outlier stars at $[\text{Fe}/\text{H}] \gtrsim -0.5$ are likely heated stars from the in-situ population. In the left panel, symbol size is inversely proportional to metallicity in order to draw attention to the low-metallicity sequence, and the average uncertainties are shown as a function of metallicity along the bottom.

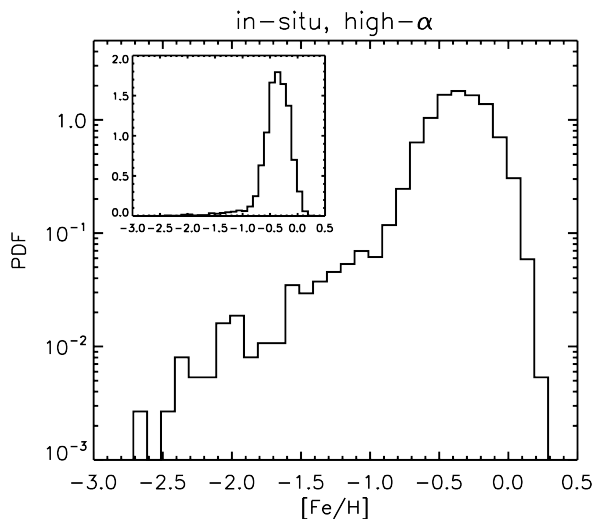


Figure 2. Metallicity distribution function (MDF) of the in-situ, high- α population. The inset shows the MDF on a linear scale. There is a substantial increase in stars above a metallicity of $[\text{Fe}/\text{H}] \approx -1.0$.

face abundances.

The spectrophotometric distances, radial velocities, and *Gaia* proper motions are used to derive a variety of quantities including projections of the angular momentum vector onto the Galactocentric coordinate system and the azimuthal velocity, V_ϕ , in spherical coordinates. We adopt the Galactocentric frame implemented in *Astropy* v4.0 (Astropy Collaboration et al. 2013, 2018). This frame is right-handed, i.e., prograde (retrograde) orbits have $L_Z < 0$ ($L_Z > 0$). Orbit-related quantities including eccentricities, e , are computed using *gaia* v1.1 (Price-Whelan 2017; Price-Whelan et al. 2017) with its default *MilkyWayPotential*. See Naidu et al. (2020) for details.

In this paper we focus on a high-quality subset of the H3 data. In particular, we require spectroscopic SNR > 20 , $\log g > 3.5$, $V_{\text{rot}} < 2 \text{ km s}^{-1}$, *Gaia* RUWE < 1.5 , and $\chi_{\text{spec}}^2/\text{DOF} < 2.5$. There are a variety of data quality flags; we require that

no flags have been set. The SNR, flag, and $\log g$ cuts reduce the sample to 9,476 stars. The RUWE cut reduces the sample to 9,163 stars, and the last two cuts result in a final sample of 8,544 stars. For this sample, the median SNR of the *Gaia* EDR3 parallax and proper motion is 17 and > 100 , respectively. The median formal uncertainties on $[\text{Fe}/\text{H}]$ and $[\alpha/\text{Fe}]$ are 0.02, although they increase toward lower metallicities such that the median uncertainties are 0.05 at $[\text{Fe}/\text{H}] = -2$.

Owing to the parallax selection of the overall survey combined with the subsequent $\log g$ and SNR selections, the distribution of $|Z|$ for this sub-sample peaks at 1.3 kpc, drops sharply at $|Z| < 0.7$ kpc, and has a tail to $|Z| \approx 4$ kpc. The sample is thus ideally suited to study the high- α disk, which has a scale-height of 0.6–1 kpc (e.g., Bovy et al. 2012).

3. RESULTS

3.1. Chemistry, kinematics, and ages of in-situ stars

We begin by separating stars into in-situ and accreted populations. These two populations are shown in Figure 1 in $[\alpha/\text{Fe}]$ vs. $[\text{Fe}/\text{H}]$. The separation is based solely on kinematic quantities, but the choice of cuts was determined by inspecting the distribution of stars in this space. In particular, the definitions were chosen such that high eccentricity stars at $[\alpha/\text{Fe}] < 0.2$ and $[\text{Fe}/\text{H}] \lesssim -0.5$ only appear in the accreted population. The accreted sample is defined by the following criteria:

$$e > 0.9 \vee (e > 0.8 \wedge L_Z > 500 \text{ km s}^{-1} \text{ kpc}^{-1}), \quad (1)$$

where e is the orbital eccentricity and L_Z is the Z -component of the angular momentum vector (recall that $L_Z > 0$ means retrograde orbits in our convention). The in-situ population is defined by:

$$e < 0.8 \wedge L_Z < 0 \text{ km s}^{-1} \text{ kpc}^{-1}. \quad (2)$$

We also remove one star that has an orbit apocenter $r_{\text{apo}} > 30$ kpc. The union of these two selections does not cover all of parameter space - there is a transition region containing an overlap of accreted and in-situ stars (7% of the sample). The ≈ 7 metal-rich stars in the accreted sample at $[\text{Fe}/\text{H}] \gtrsim -0.6$

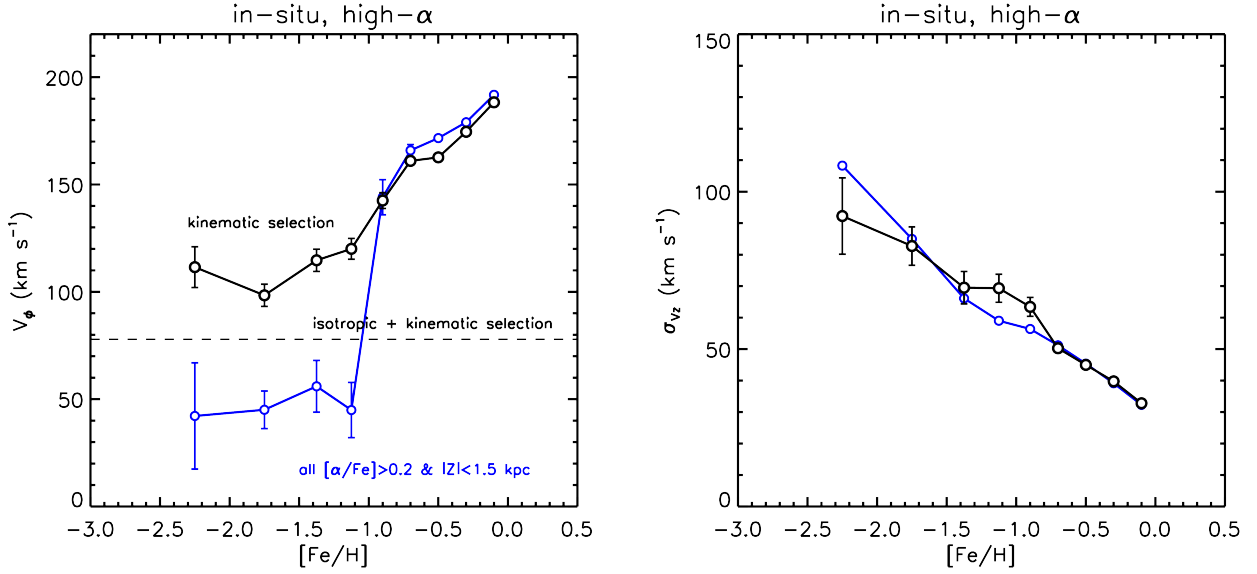


Figure 3. Average kinematic behavior of the in-situ, high- α population as a function of metallicity. Left panel: average azimuthal velocity (V_ϕ). Right panel: vertical velocity dispersion (σ_{vz}). Our kinematic selection of the in-situ sample (black line) is compared to a sample selected only to have high α and $|Z| < 1.5$ kpc (blue line). The former selection will bias the azimuthal velocity high because stars on retrograde and radial orbits are removed, while the latter will bias the velocity low because some accreted stars, which have preferentially radial orbits, are included. The true azimuthal velocity of the in-situ population lies in between the black and blue lines. Below a metallicity of $[\text{Fe}/\text{H}] \approx -1$ the population is kinematically hot with little net rotation; at higher metallicities the population is increasingly cold and disk-like. We include in the left panel a dashed line that indicates the average value for an intrinsically isotropic velocity distribution with the in-situ sample selection applied.

are likely heated stars from the in-situ population (they mostly overlap with the metal-rich, high- α in-situ population). For reasons discussed below, it is likely that the in-situ sampled defined here is incomplete but relatively pure. Such a sample is well-suited to study abundance patterns and ages.

In principle there could be accreted stars on prograde orbits that would contaminate our in-situ selection. To test this possibility, we have divided our in-situ sample into low and moderate-eccentricity subsamples ($e < 0.4$ and $e > 0.6$). These two sub-populations trace the same sequence in abundance space. It is unlikely that an accreted population would have the same distribution in abundance-eccentricity space as the in-situ population, so we conclude from this test that contamination of the in-situ population by accreted stars is low.

Figure 1 demonstrates that in-situ (prograde) stars span the full range of metallicities probed by H3. Importantly, the sequence of stars at high α smoothly extends from low metallicities to the traditional high- α locus at $[\text{Fe}/\text{H}] > -0.5$ and $[\alpha/\text{Fe}] > 0.2$. In detail, the chemistry of the high- α sequence is complex and shows three distinct regimes: declining $[\alpha/\text{Fe}]$ with increasing metallicity at $[\text{Fe}/\text{H}] \lesssim -1.3$; rising $[\alpha/\text{Fe}]$ to $[\text{Fe}/\text{H}] \approx -0.7$, and declining $[\alpha/\text{Fe}]$ again for $[\text{Fe}/\text{H}] \gtrsim -0.7$. This non-monotonic chemical track is the primary observational result of this paper.

In the rest of this paper we focus on the high- α subset of the in-situ population. We define the high- α sequence as $[\alpha/\text{Fe}] > -0.06$ $[\text{Fe}/\text{H}] + 0.18$ for $[\text{Fe}/\text{H}] > -0.9$ (indicated by the grey line in the left panel of Figure 1) and all in-situ stars at $[\text{Fe}/\text{H}] \leq -0.9$. The results below are unchanged if we adopt a simpler selection of $[\alpha/\text{Fe}] > 0.2$ for the high- α population.

Figure 2 shows the metallicity distribution function (MDF) of the in-situ high- α stars. The H3 selection function (being a function of parallax and magnitude) is nearly unbiased with respect to metallicity. We therefore interpret the observed MDF as a fair representation of the true underlying MDF in the volume probed by the sample. One clearly sees

a rapid increase in the number of stars in this population at $[\text{Fe}/\text{H}] \gtrsim -1.0$. Only 4% of stars in the in-situ high- α population have $[\text{Fe}/\text{H}] < -1.0$ and only 1% have $[\text{Fe}/\text{H}] < -1.3$, (in good agreement with Belokurov & Kravtsov 2022, who find 1% of in-situ stars have $[\text{Fe}/\text{H}] < -1$).

Figure 3 shows the average kinematic behavior of the in-situ high- α population as a function of metallicity. In this figure we have relaxed the SNR threshold from 20 to 15, which increases the sample from 8,544 to 17,565 stars. The kinematic uncertainties remain small at lower SNR, allowing us to increase the sample size here. The left panel shows the average azimuthal velocity (V_ϕ) versus metallicity while the right panel shows the vertical velocity dispersion versus metallicity. The left panel displays two clear regimes: at $[\text{Fe}/\text{H}] \lesssim -1$ the kinematic behavior is constant, while at $[\text{Fe}/\text{H}] \gtrsim -1$ the population becomes increasingly well-ordered (and kinematically colder) toward higher metallicities. This change in behavior of the kinematics at $[\text{Fe}/\text{H}] \approx -1$ is in good agreement with Belokurov & Kravtsov (2022). The trend at $[\text{Fe}/\text{H}] \gtrsim -1$ is broadly in agreement with previous work (e.g., Lee et al. 2011; Re Fiorentin et al. 2019; Han et al. 2020).

Our in-situ population is defined to be prograde ($L_z < 0$) and have $e < 0.8$, so care must be taken when interpreting the kinematics of this population. To provide some guidance, we have performed two tests. First, in Figure 3 we compare the standard kinematic selection of the in-situ stars (black lines) to a selection based solely on chemistry ($[\alpha/\text{Fe}] > 0.2$) and height from the Galactic plane ($|Z| < 1.5$ kpc; blue lines). We can see from Figure 1 that the chemistry cut retains nearly all of the in-situ high- α sequence, while removing the metal-rich end of the accreted population. The cut on Z is designed to remove additional accreted stars, as they extend to larger $|Z|$ than the kinematically-selected in-situ stars. We expect the kinematic selection to bias the resulting average velocities high, as in-situ stars on retrograde or radial orbits are removed, while the chemistry and spatial selection will bias the

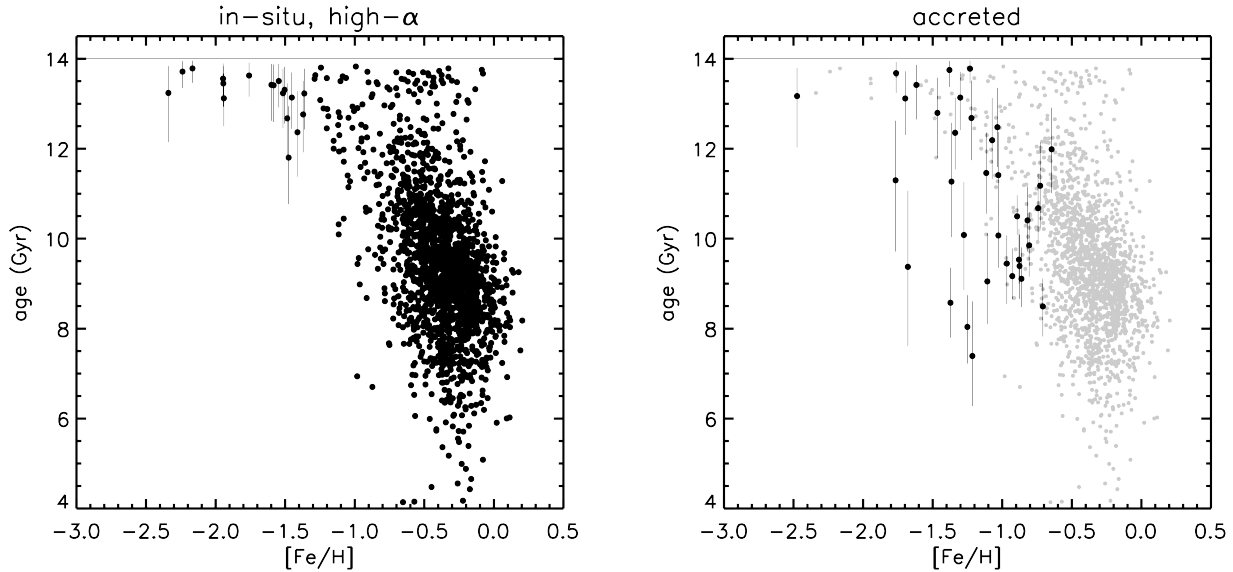


Figure 4. Ages of the in-situ, high- α (left panel) and accreted (right panel) stars as a function of metallicity. The sample here is restricted to main sequence turnoff and subgiant stars ($3.8 < \log g < 4.2$) where age estimates are most reliable. The upper limit on allowed ages is 14 Gyr (solid line). Error bars represent formal 68% confidence intervals; in the left panel they are shown only at $[\text{Fe}/\text{H}] < -1.3$ for clarity. In the right panel, the in-situ stars are shown as light grey points for direct comparison. The in-situ, high- α population is uniformly very old at $[\text{Fe}/\text{H}] \lesssim -1.3$, with ages $\gtrsim 12$ Gyr. At metallicities above $[\text{Fe}/\text{H}] \approx -1$ the ages span a wide range, from ≈ 8 –12 Gyr. In contrast to the in-situ population, the accreted population contains stars younger than 12 Gyr even at low metallicities.

velocities low, as there will be contamination from accreted stars, which preferentially have radial orbits. The true average velocity of the in-situ stars should lie in between these two limits. The key point for this paper is that the azimuthal velocity changes abruptly at $[\text{Fe}/\text{H}] \approx -1$.

As a second test, we have taken the Rybizki et al. (2018) mock stellar catalog and selected stars with $\log g > 3.5$ and applied our in-situ selection ($e > 0.8$ and $L_Z < 0$) as well as the H3 window function. We then computed the average azimuthal velocity for the halo component of this mock catalog, which intrinsically has no net rotation and a nearly isotropic velocity ellipsoid. This is shown as a dashed line in the left panel of Figure 3. Even at the lowest metallicities the fiducial kinematic selection (black line) has average velocities in excess of the null expectation. For this test to be informative, the underlying in-situ velocity ellipsoid would need to be similar to that assumed in the mock catalog. Belokurov & Kravtsov (2022) measure dispersions from their low-metallicity in-situ sample of $\sigma \approx 80$ –90 km s^{-1} in the R , Z , and ϕ components, while the Rybizki et al. (2018) model assumes $\sigma_R = 141 \text{ km s}^{-1}$, $\sigma_Z = 75 \text{ km s}^{-1}$, and $\sigma_\phi = 75 \text{ km s}^{-1}$. While not identical, these values are quite close, especially in Z and ϕ , and so we conclude that this test is reliable. From these two tests we infer that there is evidence for modest net rotation of the low-metallicity in-situ population with $V/\sigma \lesssim 1$.

In Figure 4 we show the age-metallicity relation for the in-situ high- α (left panel) and accreted (right panel) populations. For this figure we restrict the sample to stars with $3.8 < \log g < 4.2$ (i.e., the main sequence turnoff and subgiant branch), where the age constraints are most precise. The median formal uncertainty on log age in this regime is 0.03. Assumptions in the isochrones are the dominant source of systematic uncertainty, which we do not attempt to quantify here. However, we emphasize that any change to the underlying stellar models is more likely to produce a produce an overall shift in ages at a given metallicity, rather than an increase

in the scatter. For the accreted population we also remove the seven most metal-rich stars that are likely contamination from the in-situ population and are visible in the right panel of Figure 1.

Figure 4 shows that the in-situ population is remarkably old at $[\text{Fe}/\text{H}] \lesssim -1.3$, with ages almost exclusively > 12 Gyr, and a median age of 13.3 Gyr (implying a formation epoch of $z > 4$). Moreover, the range in ages at low metallicity is very small - the dispersion is 0.5 Gyr, which is comparable to the average uncertainty. In other words, the data are consistent with the low-metallicity in-situ stars having formed over a very short interval 13.3 Gyr ago. This is in stark contrast to the accreted population, which has a much broader age distribution even at low metallicities. This comparison shows that metal-poor stars are not always maximally old and that MINESweeper is able to distinguish between old (10–12 Gyr) and very old (> 12 Gyr) ages. At metallicities above $[\text{Fe}/\text{H}] \approx -1$ the ages of the high- α in-situ population span a much wider range, from ≈ 8 –12 Gyr.

There is an interesting population of stars with ages $\gtrsim 13$ Gyr and $[\text{Fe}/\text{H}] > -1$ that is offset from the main locus at 8–12 Gyr. These old, metal-rich stars appear in other samples as well (e.g., Edvardsson et al. 1993; Bensby et al. 2014). We have inspected the MINESweeper fits of these stars and see no obvious problems. We speculate that unresolved binaries could move stars slightly brighter and redder, thereby producing spuriously old ages around the main sequence turnoff. The *Gaia* RUWE parameter has been previously used to identify unresolved binaries (Belokurov et al. 2020a). Our parent sample already has a RUWE < 1.5 cut applied. We note that this population of ancient metal-rich stars has a higher mean RUWE than the overall sample (1.07 vs. 1.02), and plotting only stars with RUWE < 1.02 removes a large fraction of this population from Figure 4. Further inspection of this sample is warranted.

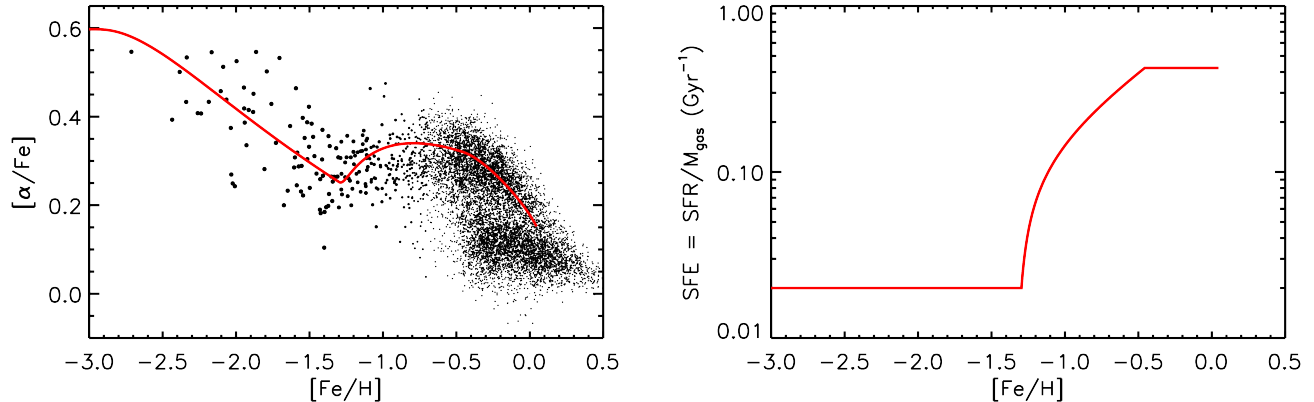


Figure 5. Chemical evolution modeling of the in-situ, high- α population. The red line shows a model in which the SFR is related to the gas mass by the star formation efficiency, whose behavior is shown in the right panel. The model has a constant gas inflow rate and a mass-loading factor $\eta \equiv \dot{M}_{\text{out}}/\text{SFR} = 2$. The key point is that the change in chemical evolution track around $[\text{Fe}/\text{H}] \approx -1.3$ is driven by a large increase in the star formation efficiency.

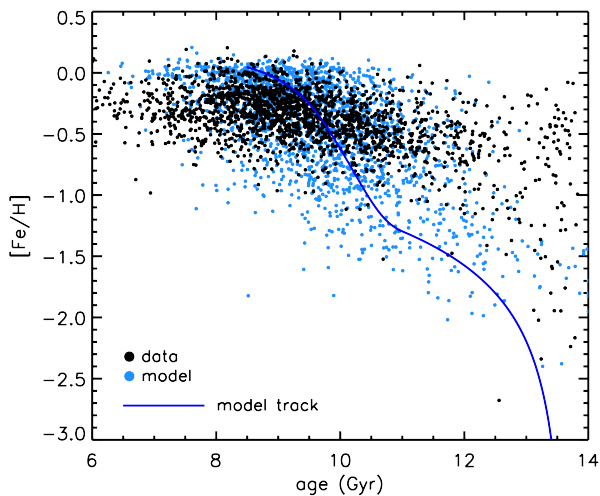


Figure 6. Age-metallicity relation comparing the in-situ, high- α data and the chemical evolution model. In addition to the (noiseless) model track, we have sampled the model according to the star formation history and applied measurement uncertainties in both age and metallicity to mimic the data. The model produces stars ≈ 1 Gyr younger than the data at $[\text{Fe}/\text{H}] < -1.3$ but is otherwise in reasonable agreement with the data.

3.2. A Chemical Evolution Model

In this section we employ a chemical evolution model to interpret the abundance pattern of the in-situ high- α population. We use the VICE program (Johnson et al. 2020), which is a flexible package for computing chemical evolution models for a wide range of input physics (inflows, outflows, varying star formation efficiencies and yields, etc.). In particular, we are motivated by Weinberg et al. (2017) to consider changes in the star formation efficiency timescale, τ_* , defined as the gas mass divided by the star formation rate: $\tau_* \equiv M_{\text{gas}}/\text{SFR}$. Abrupt changes in τ_* can result in non-monotonic behavior in $[\alpha/\text{Fe}]$ vs. $[\text{Fe}/\text{H}]$ (e.g., Weinberg et al. 2017; Johnson et al. 2020), qualitatively similar to what we observe in the data (Figure 1). Below we refer to the star formation efficiency (SFE $\equiv \tau_*^{-1}$), which is simply the inverse of τ_* .

The dimensionality and uncertainty in chemical evolution models is large and includes yields from core-collapse (CC)

supernovae (SNe) and Type Ia SNe, the delay time distribution of Type Ia SNe, parameterized functions for the gas inflow and outflow rates and SFRs, and the metallicity of the outflows and inflows. Motivated by Johnson et al. (2020), we choose to parameterize the model in terms of the SFE timescale and evolution of the gas mass with time. The SFR is inferred from these two quantities. The model starts with no gas and has a constant inflow rate of zero metallicity gas: $\dot{M}_{\text{gas}} = 5 M_{\odot} \text{yr}^{-1}$. The normalization of the inflow rate has no effect on the tracks in chemistry space and only affects the amplitude of the SFR.

We adopt the following IMF-averaged Mg and Fe yields for CC and Ia SNe: $y_{\text{Mg}}^{\text{CC}} = 0.0026$, $y_{\text{Fe}}^{\text{CC}} = 0.0012$, $y_{\text{Mg}}^{\text{Ia}} = 0.0$, $y_{\text{Fe}}^{\text{Ia}} = 0.003$. These yields follow Johnson et al. (2020), except that we increase the Type Ia Fe yield to better reproduce the slope of $[\text{Mg}/\text{Fe}]$ vs. $[\text{Fe}/\text{H}]$ at low metallicity (Johnson et al. adopt $y_{\text{Fe}}^{\text{Ia}} = 0.0017$). We adopt IMF-averaged yields rather than individual star yields because we do not expect star formation and mixing to be so well-organized in the chaotic early Galaxy. We therefore assume that IMF sampling effects will create scatter, rather than a systematic trend, in the abundance pattern. CC yields are uncertain because of effects in massive star evolution, explosive nucleosynthesis, and which stars collapse to form black holes rather than exploding (see discussion in Griffith et al. 2021). SNIa Fe yields are uncertain mainly because of uncertainties in the normalization of the SNIa rate (see Maoz & Graur 2017). Abundance ratios depend primarily on yield ratios, so here we are adjusting yields within plausible ranges to match the observed abundance ratio trends. Changing all yields by the same multiplicative factor is largely degenerate with changing the outflow efficiency (Weinberg et al. 2017). Our most important assumption is that the IMF-averaged yield ratios are metallicity independent in the regime of interest, so that the trends of $[\alpha/\text{Fe}]$ vs. $[\text{Fe}/\text{H}]$ seen in Figure 1 reflect evolution in the ratio of CC to Ia enrichment, not changes in yields. We return to this point in Section 4.1.

We consider a model that has outflows with a mass-loading factor $\eta \equiv \dot{M}_{\text{out}}/\text{SFR} = 2$ where \dot{M}_{out} is the mass outflow rate. The outflows are assumed to have the same metallicity as the star-forming gas. If we assumed that outflows preferentially ejected CC products, we would require lower $y_{\text{Fe}}^{\text{Ia}}$ to obtain

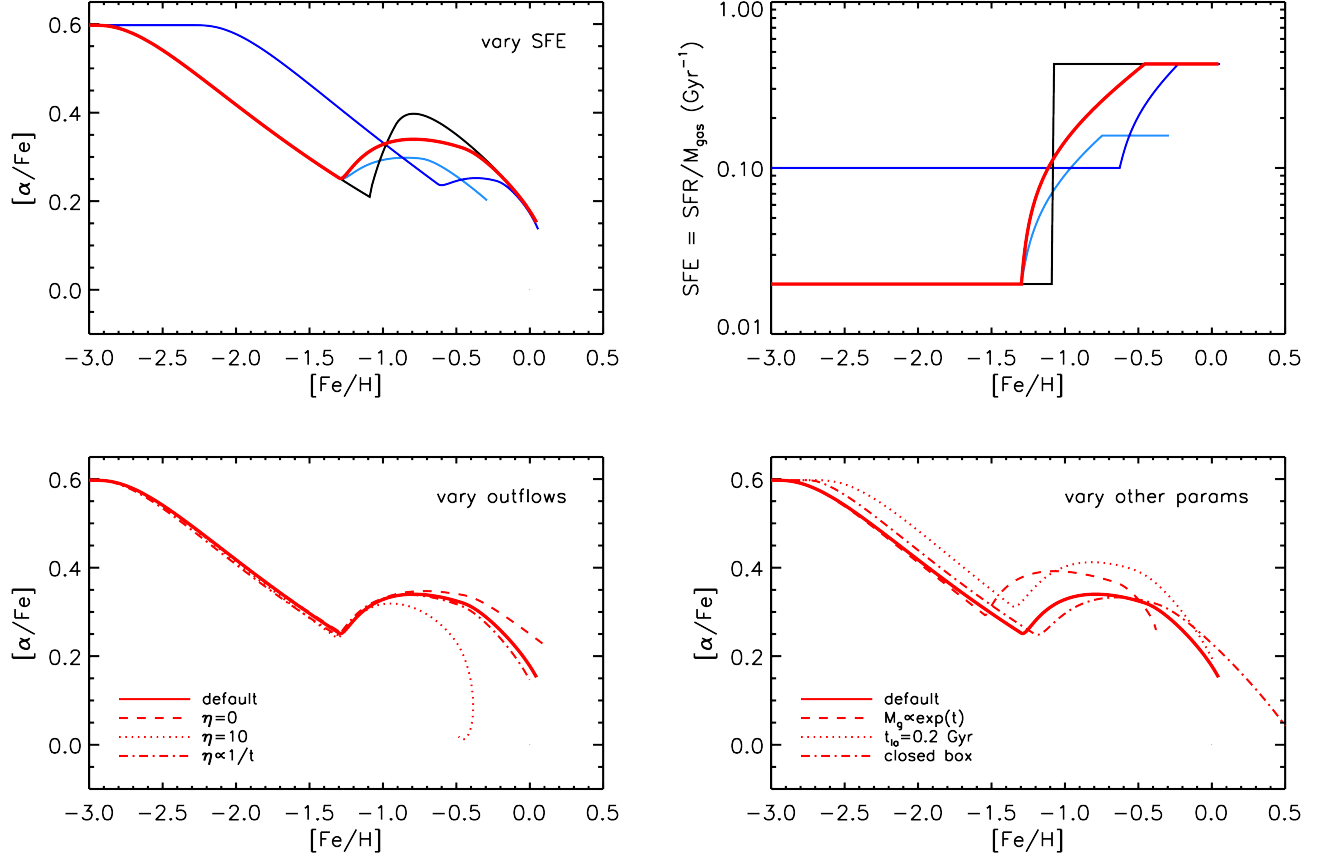


Figure 7. Variations to the default chemical evolution model. The top left panel shows the effect of varying the SFE on the abundance tracks; the corresponding SFEs are shown in the top right panel. The bottom left panel shows variations in the mass-loading factor, η , where the default is $\eta = 2$. The variations in η are large and include a time-dependent mass-loading factor. The bottom right panel shows changes in the gas inflow rate ($M_g \propto e^t$), an increase in the minimum SNIa time (from 0.1 to 0.2 Gyr), and the adoption of a closed box model (all gas is present at $t = 0$ with no inflows or outflows).

similar $[\alpha/\text{Fe}]-[\text{Fe}/\text{H}]$ evolutionary tracks. In our model, we interpret the downward trend in $[\alpha/\text{Fe}]$ between $[\text{Fe}/\text{H}] = -2.5$ and -1.3 as a consequence of increasing SNIa enrichment. Because the timescale for this enrichment is long – for a standard delay time distribution, a stellar population produces half of its Type Ia SNe in about 1 Gyr – the SFE during this phase must be very low so that the population does not evolve past $[\text{Fe}/\text{H}] = -1.3$. We interpret the rise in $[\alpha/\text{Fe}]$ between $[\text{Fe}/\text{H}] = -1.3$ and -0.7 as a consequence of accelerating star formation, which increases the rate of CC enrichment relative to Ia enrichment. To achieve a good fit to the observed trend, we adopt the following functional form for τ_* (in units of Gyr):

$$\tau_* = \begin{cases} 50 & t < 2.5 \text{ Gyr} \\ 50/[1+3(t-2.5)]^2 & 2.5 \leq t \leq 3.7 \text{ Gyr} \\ 2.36 & t > 3.7 \text{ Gyr}. \end{cases} \quad (3)$$

An instantaneous decrease in τ_* at 2.5 Gyr would result in a rapid increase in $[\text{Mg}/\text{Fe}]$ at nearly fixed $[\text{Fe}/\text{H}]$ (see below, and Weinberg et al. 2017; Johnson et al. 2020). In order to match the observations we required a more gradual change; the precise function was determined by trial-and-error.

Figure 5 shows the resulting model track in $[\alpha/\text{Fe}]$ vs. $[\text{Fe}/\text{H}]$ in comparison to the data. We adopt $[\text{Mg}/\text{Fe}]$ from the model to compare with $[\alpha/\text{Fe}]$ as the H3 spectral window is mostly sensitive to Mg. The model parameters were tuned

to fit the data shown in the left panel, so the agreement there is by construction. The right panel shows the model star formation efficiency, $\tau_*^{-1} \equiv \text{SFR}/M_{\text{gas}}$ (Eq. 3) as a function of metallicity. In this model the CC yields produce a plateau in $[\text{Mg}/\text{Fe}]$ of $+0.6$, which is barely visible in Figure 5 at $[\text{Fe}/\text{H}] \approx -3$. The second plateau at $[\text{Mg}/\text{Fe}] \approx 0.3$ at higher metallicity is a consequence of the accelerated star formation rate over this interval.

The key conclusion from this model is that the non-monotonic track in the observed $[\alpha/\text{Fe}]$ vs. $[\text{Fe}/\text{H}]$ plane can be explained by a dramatic and relatively rapid – though not instantaneous – increase in the star formation efficiency. Typical values for τ_* in the local universe are ≈ 2 Gyr for the molecular gas (Leroy et al. 2008), comparable to the asymptotic value of τ_* in our model. Much higher values of τ_* could arise if most of the cold gas is in atomic form (see discussion in Johnson et al. 2020). Alternatively, a low effective τ_* could arise if metals from supernovae are ejected into the gaseous halo and thus diluted by a gas reservoir that is much larger than the reservoir that is actually forming stars (Mason et al. 2024).

A similar non-monotonic track is apparent in the two-infall+outflow chemical evolution model of Brusadin et al. (2013). In their model the non-monotonic behavior is the result in a significant period (1–2 Gyr) in which there is no star formation. Micali et al. (2013) also report non-monotonic be-

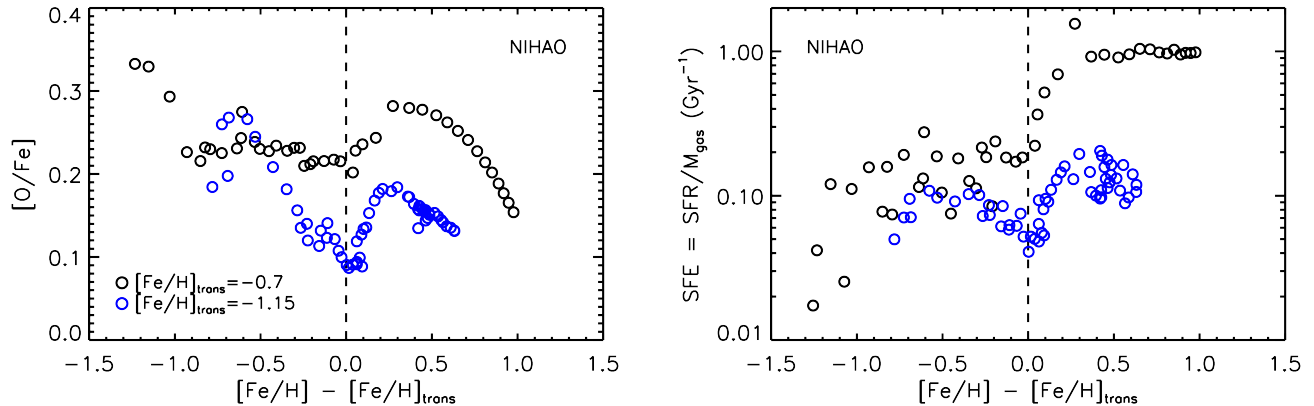


Figure 8. Comparison to simulations from the NIHAO project. Left panel: $[O/Fe]$ vs. metallicity for two galaxies that show non-monotonic abundance behavior (g7.66e11 in black and g3.59e11 in blue). Right panel: star formation efficiency (SFE) vs. metallicity for these two galaxies. In each panel, the metallicity is shown relative to the metallicity at which the non-monotonic transition occurs (labeled $[Fe/H]_{trans}$). The sudden rise in $[O/Fe]$ at the transition scale is clearly associated with a rise in SFE in both simulated galaxies. This provides additional support for our interpretation of the observed non-monotonic abundance trends in terms of an increase in SFE.

havior in their three-infall chemical evolution model, in which the halo, thick disk, and thin disk components form via three distinct infall episodes. In their model the non-monotonic behavior is explicitly linked to a rapid increase in star formation efficiency. Alternatively, motivated partly by the preprint version of our paper, Chen et al. (2023) present a scenario in which the non-monotonic evolution of $[\alpha/Fe]$ is triggered by a rapid acceleration of the gas inflow rate.

Figure 6 shows the age-metallicity relation comparing the data and chemical evolution model. The mock track is shown as a solid line, and we also include a realization of the model by drawing model stars proportional to the star formation history and then applying observational uncertainties. There is reasonable agreement at $[Fe/H] > -1.3$ but at lower metallicities the model is approximately 1 Gyr too young. The model was not fit to the ages, so the poor agreement is perhaps not surprising.

Figure 7 shows the effect of various model parameters on the model $[\alpha/Fe]$ vs. $[Fe/H]$ track. The top panels show the effect of varying the SFE (left panel is the abundance plane, right panel is the SFE). As expected, an instantaneous change in SFE results in a sharp upward transition in abundance space. Models with larger SFE at early times result in a longer plateau phase at low metallicity and a much less pronounced non-monotonic feature at high metallicity. Models with a lower SFE at late times also produce a less pronounced non-monotonic feature.

In the lower left panel of Figure 7 we consider the effect of the mass-loading factor on the abundance tracks. Constant values of $\eta = 0$ (no outflows) and $\eta = 10$ (high outflows) only affect the behavior at high metallicity. A time-varying model in which $\eta(t) = 10(t+0.1 \text{ Gyr})^{-1}$ is also shown, and produces a very similar track as the default model. This strongly varying η is roughly equivalent to $\eta \propto M_*^{-0.5}$, where M_* is the model galaxy stellar mass in the adopted model.

The lower right panel of Figure 7 shows additional model variations, including a model with closed box chemical evolution (no outflows or inflows), a shift in the onset of SNe Ia from 0.1 to 0.2 Gyr, and a model in which the gas inflow rate is an exponentially increasing function of time ($M_g(t) = e^{t/1 \text{ Gyr}}$). All of these variations produce modest shifts in the abundance

tracks. We therefore conclude that none of them are able to mimic the non-monotonic behavior produced by SFE variations.

Our default model is meant to be illustrative. Unsurprisingly, it does not reproduce other aspects of the data. In particular, the predicted age-metallicity relation is too shallow (see Figure 6) and the onset of the transition to high star formation efficiency is too late. Furthermore, the distribution function (MDF) becomes shallower at $[Fe/H] > -1$, in contrast to the data, which becomes steeper. These two shortcomings are likely related. For example, a time-dependent inflow rate will generally have a small effect on the $[\alpha/Fe]$ - $[Fe/H]$ tracks (see Figure 7, and Andrews et al. 2017) but a large effect on the age-metallicity relation and the MDF. Simultaneously reproducing these key constraints will provide important insights into the early history of the Galaxy (see e.g., Kobayashi et al. 2020; Snaith et al. 2022, for recent examples), and will be the subject of future work.

3.3. Comparison to Simulations

In this section we provide a brief comparison to simulations from the NIHAO project (Wang et al. 2015). Buck (2020) showed that many simulated NIHAO galaxies display non-monotonic abundance trends, qualitatively similar to what we find in the H3 in-situ population. Two striking examples are g3.59e11 and g7.66e11, which have halo masses of $3.59 \times 10^{11} M_\odot$ and $7.66 \times 10^{11} M_\odot$, respectively. For these galaxies we have computed the average stellar metallicity ($[Fe/H]$), oxygen-to-iron abundance ratio ($[O/Fe]$), SFR averaged over 200 Myr timescales, and the gas mass as a function of time. These averages were computed for the high- α sequences defined in Buck (2020). NIHAO does not track Mg, so we use O as a tracer for α elements (though see Buck et al. 2021, for an updated stellar evolution model).

In Figure 8 we show the abundance patterns of these two galaxies (left panel) and their star formation efficiencies (right panel). We plot these quantities as a function of the metallicity relative to the metallicity at which the non-monotonic behavior begins (referred to as $[Fe/H]_{trans}$). The key point is that the rise in $[O/Fe]$ corresponds to a sudden and significant increase in star formation efficiency. We take this result

to corroborate our interpretation of the data based on analytic chemical evolution models, in which the non-monotonic behavior in $[\alpha/\text{Fe}]$ vs. $[\text{Fe}/\text{H}]$ is due to a sudden increase in star formation efficiency. Similar non-monotonic behavior is seen in other recent simulations (e.g., Few et al. 2014; Brook et al. 2020).

The transition scale occurs at a metallicity that is somewhat too high compared to the data (-0.7 and -1.15 compared to -1.3), and much too late (6 Gyr for both simulated galaxies, compared to ≈ 1 Gyr in the data). Moreover, the shape of the chemical evolution track shows quantitative differences compared to the data. Of the 35 NIHAO galaxies presented in Buck (2020), only one shows a transition at the low metallicity seen in the data ($g5.31e11$). This result is in agreement with Belokurov & Kravtsov (2022), who find that the transition between hot and cold kinematics occurs too late in the Latte (Wetzell et al. 2022) and Auriga (Grand et al. 2018b) simulations. For the NIHAO simulations, mergers appear to be the main driver of the enhanced star formation efficiency and non-monotonic abundance behavior. However, given that the timing is very different between simulations and data, we reserve judgement on the physical mechanism responsible for the transition in the data to future work.

4. DISCUSSION

4.1. Caveats & Limitations

Before placing these results in context, we highlight several caveats and limitations to the present analysis.

The H3 window function is uniform and nearly complete at $|b| > 30^\circ$ and $\text{Dec.} > -20^\circ$. Existing H3 data does not reach lower Galactic latitudes, and the parallax selection removes most stars with heliocentric distances of $\lesssim 1$ kpc. For the high- α population studied here, which has a scale-height of $0.6\text{--}1$ kpc (e.g., Bovy et al. 2012), the lack of in-plane coverage of H3 is unlikely to bias our results, but we caution that any systematic population variation between $|Z| < 1$ kpc and $|Z| > 1$ kpc would not be reflected in our results.

Our abundance determinations are based on plane-parallel 1D atmospheres and assumed LTE. Furthermore, our α abundances are primarily derived from the Mg I triplet at 5167, 5173, 5183Å, which is very strong and sensitive to the structure of the upper stellar atmospheres (e.g., Bergemann et al. 2017a). Cargile et al. (2020) showed that the H3 abundance scale (in both $[\text{Fe}/\text{H}]$ and $[\alpha/\text{Fe}]$) agrees well with literature values for globular and open clusters spanning the metallicity range $[\text{Fe}/\text{H}] \approx -2.3$ to $+0.0$. Furthermore, as we show in Appendix A, the trends we identify in abundance space are also seen in the APOGEE data. This comparison gives added confidence to our use of the Mg I triplet for abundance determination. Furthermore, the comparison between the in-situ and accreted sequences in Figure 1 – which are on the same abundance scale – shows that there is a feature in the in-situ abundances at $[\text{Fe}/\text{H}] \approx -1.3$ that does not appear in the accreted sample. This feature therefore cannot be due to deficiencies in the H3 abundance analysis. Nonetheless, we caution that the detailed quantitative behavior in abundance space is sensitive to NLTE and 3D atmosphere effects (see e.g., Bergemann et al. 2017b), and the overall behavior of the $[\alpha/\text{Fe}]$ vs. $[\text{Fe}/\text{H}]$ sequence at low metallicity differs across the literature (compare Gratton et al. 2003; Cayrel et al. 2004; Ruchti et al. 2011; Bensby et al. 2014). Our quantitative interpretation of the de-

tailed abundance behavior at low metallicity must therefore be treated with care.

The most important observational caveat in this work is the separation of in-situ and accreted stars at low metallicity. Despite decades of effort, this task remains challenging (see e.g., Buder et al. 2022). Following the work of Hawkins et al. (2015), Belokurov & Kravtsov (2022) use $[\text{Al}/\text{Fe}]$ to separate in-situ and accreted populations. While this selection provides good separation at $[\text{Fe}/\text{H}] \gtrsim -1.2$, at lower metallicities the in-situ population overlaps in chemical space with the accreted stars, in both the diagnostic $[\text{Al}/\text{Fe}]$ and $[\text{Mg}/\text{Mn}]$ abundance ratios, as we show in Appendix B (and also discussed in Horta et al. 2021; Belokurov & Kravtsov 2022). This means that it will be challenging to identify in-situ stars at low metallicity purely on the basis of these proposed diagnostic abundance ratios. However, our approach in this work, which employs kinematic selection, is also problematic. In-situ stars on highly radial or retrograde orbits, which exist at low metallicity (Belokurov & Kravtsov 2022), will be missed by our selection. Our results related to the kinematic behavior of the in-situ population (Figure 3) must therefore be interpreted with care, as we discuss in Section 3.1. A path forward may involve exploiting the predicted spatial variation in the accreted and in-situ populations with height from the Galactic plane in order to decompose these two populations, at least in a statistical sense.

In order to interpret the chemical behavior of the in-situ population we relied on an analytic chemical evolution model. The chemical evolution of a system is very complex and challenging to model as there are many relevant physical processes, each with significant uncertainties (including stellar yields, Type Ia delay time distribution, inflow and outflow rates, mass-loading, mixing, etc.). Within the one-zone framework considered in Section 3.2, we undertook a wide exploration of the parameter space and could not identify another physical mechanism besides a change in SFE that would reproduce the observed non-monotonic behavior in $[\alpha/\text{Fe}]$ vs. $[\text{Fe}/\text{H}]$.

The most obvious alternative way to produce the non-monotonic behavior is with metallicity-dependent CC yields (e.g., Heger & Woosley 2010; Vincenzo et al. 2016). However, we do not see any sign of this behavior in our accreted star sample (which shows a smooth decline in $[\alpha/\text{Fe}]$ over the range $-2 \lesssim [\text{Fe}/\text{H}] \lesssim -0.5$), and the variable SFE model reproduces the distinctive shape of the observed trend remarkably well (Figure 5). Further high-precision studies of large samples in this metallicity range would be valuable for detecting or ruling out metallicity-dependent yields, which should be governed by stellar astrophysics with little dependence on galactic environment. Conversely, measuring other elements with large contributions from SN Ia or from AGB stars could be a useful way of verifying that the early decline of $[\alpha/\text{Fe}]$ is indeed a result of a time-delayed enrichment source.

4.2. The High- α Disk from Beginning to End

We begin with a summary of the main results. We identified a sample of in-situ stars by selecting prograde orbits with eccentricities $e < 0.8$. We argue that this selection results in a relatively pure but incomplete sample of in-situ stars at low metallicity. The high- α subset of these stars forms a continuous sequence in $[\alpha/\text{Fe}]$ vs. $[\text{Fe}/\text{H}]$. This sequence is non-monotonic, showing inflections at $[\text{Fe}/\text{H}] \approx -1.3$ and ≈ -0.7 . Both analytic chemical evolution models and realistic hydrodynamic simulations show that this non-monotonic be-

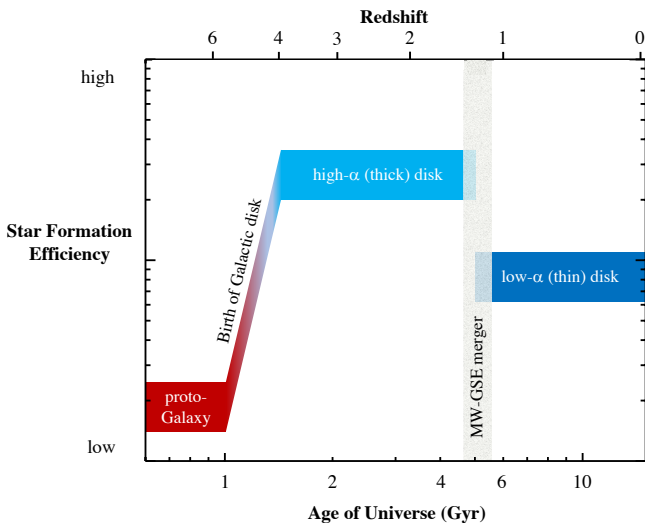


Figure 9. Schematic overview of Galactic star formation efficiency (SFE) over cosmic time. The colors indicate the kinematic state of the forming component (red = hot, blue = cold). At early times the proto-Galaxy has low SFE and is kinematically hot. After a period of ~ 1 Gyr, the SFE rapidly increases and the kinematics become much colder. This marks the beginning of the high- α disk phase. At $z \sim 1$ the GSE finishes merging with the Galaxy. This event truncates the high- α disk, creates the in-situ halo via kicked up high- α disk stars, and initiates the epoch of low- α disk formation. In this final phase, the kinematics are colder and the SFE lower than the high- α disk (Nidever et al. 2014). Epochs are approximate. See text for details.

havior is a reflection of a substantial increase in star formation efficiency ($\text{SFR}/M_{\text{gas}}$). The kinematics of the high- α in-situ population are hot with small net rotation ($V/\sigma \lesssim 1$) at $[\text{Fe}/\text{H}] \lesssim -1$ and become increasingly well-ordered and cold at higher metallicities. Main sequence turnoff-based ages show stars at $[\text{Fe}/\text{H}] \lesssim -1.3$ are uniformly very old (≈ 13 Gyr), while more metal-rich stars span a range of ages ($\approx 8-12$ Gyr).

The fact that the abundance pattern forms a continuous sequence from $[\text{Fe}/\text{H}] \approx -2.5$ to ≈ 0 , combined with the observed age-metallicity relation, supports a picture in which the low-metallicity prograde stars are both genuinely in-situ and represent the earliest epochs of the Galaxy. The continuity in abundance space argues against an accretion origin for the low-metallicity stars (cf. Abadi et al. 2003; Carollo et al. 2019). This non-monotonic abundance behavior is not unique to the Galaxy (e.g., Hendricks et al. 2014; Nidever et al. 2020; Hasselquist et al. 2021), and suggests that abrupt star formation efficiency variations are common.

Observations are providing an increasingly sharp view of the high- α disk from the earliest epochs to the present day. However, the extant data do not uniquely determine the physical origin and evolution of this Galactic component. Here we sketch one plausible scenario that is consistent with the existing data. We propose that the ancient, metal-poor in-situ stars represent the earliest epoch of the proto-Galaxy. During this “simmering phase”, the star formation efficiency was low and relatively few stars formed. After ≈ 1 Gyr of simmering, at a critical metallicity of $[\text{Fe}/\text{H}] \approx -1.3$, the Galaxy underwent a dramatic transition to a “boiling phase”, in which the star formation efficiency substantially increased, the number of stars increased, and the kinematics became increasingly cold and disk-like (Belokurov & Kravtsov 2022, refer to this as the “spin-up” phase). This transition marks the birth of the Galactic disk. The boiling phase – the epoch of the high- α disk – lasted for $\approx 3-4$ Gyr (from $z \approx 4$ to $z \approx 1$), at which time a

merger with GSE created the in-situ halo from dynamically-heated disk stars, terminated the high- α disk phase, and initiated growth of the low- α disk (e.g., Bonaca et al. 2020; Belokurov et al. 2020b). The low- α disk is kinematically colder and consistent with having formed at lower star formation efficiency than the high- α disk (e.g., Nidever et al. 2014). The development of a stable hot gaseous halo may also have occurred at $z \sim 1$ and regulated the delivery of gas to the star-forming disk, enabling the formation of a kinematically cold disk (e.g., Yu et al. 2021; Stern et al. 2021; Gurvich et al. 2022; Hafen et al. 2022). Perhaps it was the merger with GSE that resulted in the formation of the Milky Way’s hot halo. A schematic illustration of these key phases is shown in Figure 9. In a single-zone model, resetting the low- α disk to low metallicity requires dilution by a large influx of gas (e.g., Chiappini et al. 1997), but this requirement may be softened in multi-zone models that combine a Galactic metallicity gradient with radial migration (e.g., Schönrich & Binney 2009; Minchev et al. 2013; Loebman et al. 2016; Sharma et al. 2021; Johnson et al. 2021).

We can place a limit on the mass of the proto-Galaxy by noticing that stars at $[\text{Fe}/\text{H}] < -1.3$ comprise only 1% of the high- α in-situ population (Figure 2). Adopting a thick disk stellar mass of $6 \times 10^9 M_{\odot}$ (Bland-Hawthorn & Gerhard 2016), and equating the thick and high- α disk leads us to infer a stellar mass of the proto-Galaxy at $z \approx 4$ of $\sim 6 \times 10^7 M_{\odot}$. Such objects should be within range of upcoming *James Webb Space Telescope* (*JWST*) programs (e.g., Williams et al. 2018).

As noted in Section 4.1, it is challenging to identify in-situ stars at low metallicity. Our approach here relied on kinematic separation. Belokurov & Kravtsov (2022) selected in-situ stars based on $[\text{Al}/\text{Fe}]$ from APOGEE. They identified a significant change in the kinematic behavior of in-situ stars at $[\text{Fe}/\text{H}] \approx -1$, in good agreement with what we find here, which they interpret as the period of disk spin-up. Belokurov & Kravtsov lacked empirical age estimates, which we employ here to identify the epoch of this transition. Furthermore, our kinematic selection of in-situ stars enabled identification of such stars to much lower metallicity than in the Belokurov & Kravtsov sample ($[\text{Fe}/\text{H}] \approx -2.5$ compared to -1.5), which allowed us to identify a non-monotonic abundance pattern and its interpretation in terms of star formation efficiency variations.

What initiated the transition from simmering to boiling ≈ 13 Gyr ago? Analysis of the NIHAO simulations suggest that mergers can induce a rapid increase in star formation efficiency. At high redshift mergers are common (Fakhouri et al. 2010), and so a merger could have been responsible for this transition. In this picture, the kinematic disorder observed at $[\text{Fe}/\text{H}] \lesssim -1$ could mark the effect of a merger (or mergers) at this epoch. Another possibility lies in the very rapid increase in galaxy mass and SFR at early times, when a galaxy transitions from essentially zero SFR to a SFR of $\sim 1-10 M_{\odot} \text{ yr}^{-1}$ within ~ 1 Gyr (e.g., Renaud et al. 2021; Belokurov & Kravtsov 2022). Perhaps in this early, rapid growth phase, the ratio of SFR and gas mass accretion rates are out of sync so that the star formation efficiency experiences a rapid increase. An alternative idea advanced by Mason et al. (2024), motivated by the EAGLE simulations, is that the effective star formation efficiency is low at early times because metals from supernovae are vented and mixed into the gaseous halo, which is not forming stars, and the efficiency grows when metals are trapped in the star-forming ISM. Chen et al. (2023) show that

non-monotonic behavior of $[\alpha/\text{Fe}]$ can be triggered by rapid changes in gas infall rate rather than efficiency. We encourage further exploration of simulations at these early epochs to understand this important phase in the evolution of our Galaxy.

The results presented in this work, in combination with recent results from Belokurov & Kravtsov (2022), mark a new era in our ability to observe in the archeological record the very earliest phases of the Galaxy. These and future observations within the Galaxy should provide powerful constraints on models of the high-redshift universe that will be complementary to forthcoming observations from *JWST*.

CC thanks Vasily Belokurov and Andrey Kravtsov for very helpful conversations and feedback on an earlier draft. CC and PC acknowledge support from NSF grant NSF AST-2107253. DHW and JWJ acknowledge support from NSF grant NSF AST-1909841. RPN acknowledges an Ashford Fellowship granted by Harvard University. TB acknowledges support by the European Research Council under ERC-CoG grant CRAGSMAN-646955. YST acknowledges financial support from the Australian Research Council through DECRA Fellowship DE220101520. We thank the Hectochelle operators and the CfA and U. Arizona TACs for their continued support of the H3 Survey.

Observations reported here were obtained at the MMT Observatory, a joint facility of the Smithsonian Institution and the University of Arizona. This paper uses data products produced by the OIR Telescope Data Center, supported by the Smithsonian Astrophysical Observatory. The computations in this paper were run on the FASRC Cannon cluster supported by the FAS Division of Science Research Computing Group at Harvard University. This research made use of the NumPy (Harris et al. 2020), pynbody (Pontzen et al. 2013) and tangos (Pontzen & Tremmel 2018) package to analyze the simulations. TB gratefully acknowledges the Gauss Centre for Supercomputing e.V. (www.gauss-centre.eu) for funding this project by providing computing time on the GCS Supercomputer SuperMUC at Leibniz Supercomputing Centre (www.lrz.de) under the project number pn29mo.

This work has made use of data from the European Space Agency (ESA) mission *Gaia* (<https://www.cosmos.esa.int/gaia>), processed by the *Gaia* Data Processing and Analysis Consortium (DPAC, <https://www.cosmos.esa.int/web/gaia/dpac/consortium>) (Gaia Collaboration et al. 2021). Funding for the DPAC has been provided by national institutions, in particular the institutions participating in the *Gaia* Multilateral Agreement. Funding for the Sloan Digital Sky Survey IV has been provided by the Alfred P. Sloan Foundation, the U.S. Department of Energy Office of Science, and the Participating Institutions. SDSS-IV acknowledges support and resources from the Center for High Performance Computing at the University of Utah. The SDSS website is www.sdss.org.

REFERENCES

- Abadi, M. G., Navarro, J. F., Steinmetz, M., & Eke, V. R. 2003, *ApJ*, 597, 21
- Abdurro'uf, Accetta, K., Aerts, C., et al. 2021, arXiv e-prints, arXiv:2112.02026
- Agertz, O., Renaud, F., Feltzing, S., Read, J. I., Ryde, N., Andersson, E. P., Rey, M. P., Bensby, T., & Feuillet, D. K. 2021, *MNRAS*, 503, 5826
- Andrews, B. H., Weinberg, D. H., Schönrich, R., & Johnson, J. A. 2017, *ApJ*, 835, 224
- Astropy Collaboration, Price-Whelan, A. M., Sipőcz, B. M., et al. 2018, *AJ*, 156, 123
- Astropy Collaboration, Robitaille, T. P., Tollerud, E. J., et al. 2013, *A&A*, 558, A33
- Belokurov, V., Erkal, D., Evans, N. W., Koposov, S. E., & Deason, A. J. 2018, *MNRAS*, 478, 611
- Belokurov, V. & Kravtsov, A. 2022, arXiv e-prints, arXiv:2203.04980
- Belokurov, V., Penoyre, Z., Oh, S., Iorio, G., Hodgkin, S., Evans, N. W., Everall, A., Koposov, S. E., Tout, C. A., Izzard, R., Clarke, C. J., & Brown, A. G. A. 2020a, *MNRAS*, 496, 1922
- Belokurov, V., Sanders, J. L., Fattahi, A., Smith, M. C., Deason, A. J., Evans, N. W., & Grand, R. J. J. 2020b, *MNRAS*, 494, 3880
- Bensby, T., Feltzing, S., & Oey, M. S. 2014, *A&A*, 562, A71
- Bergemann, M., Collet, R., Amarsi, A. M., Kovalev, M., Ruchti, G., & Magic, Z. 2017a, *ApJ*, 847, 15
- Bergemann, M., Collet, R., Schönrich, R., Andrae, R., Kovalev, M., Ruchti, G., Hansen, C. J., & Magic, Z. 2017b, *ApJ*, 847, 16
- Bird, J. C., Kazantzidis, S., Weinberg, D. H., Guedes, J., Callegari, S., Mayer, L., & Madau, P. 2013, *ApJ*, 773, 43
- Bland-Hawthorn, J. & Gerhard, O. 2016, *Annual Review of Astronomy and Astrophysics*, 54, 529
- Bonaca, A., Conroy, C., Cargile, P. A., Naidu, R. P., Johnson, B. D., Zaritsky, D., Ting, Y.-S., Caldwell, N., Han, J. J., & van Dokkum, P. 2020, *ApJL*, 897, L18
- Bonaca, A., Conroy, C., Wetzel, A., Hopkins, P. F., & Kereš, D. 2017, *ApJ*, 845, 101
- Bonaca, A., Hogg, D. W., Price-Whelan, A. M., & Conroy, C. 2019, *ApJ*, 880, 38
- Bovy, J., Erkal, D., & Sanders, J. L. 2017, *MNRAS*, 466, 628
- Bovy, J., Rix, H.-W., Liu, C., Hogg, D. W., Beers, T. C., & Lee, Y. S. 2012, *ApJ*, 753, 148
- Brook, C. B., Kawata, D., Gibson, B. K., Gallart, C., & Vicente, A. 2020, *MNRAS*, 495, 2645
- Brusadin, G., Matteucci, F., & Romano, D. 2013, *A&A*, 554, A135
- Buck, T. 2020, *MNRAS*, 491, 5435
- Buck, T., Rybizki, J., Buder, S., Obreja, A., Macciò, A. V., Pfrommer, C., Steinmetz, M., & Ness, M. 2021, *MNRAS*, 508, 3365
- Buder, S., Lind, K., Ness, M. K., et al. 2022, *MNRAS*, 510, 2407
- Cargile, P. A., Conroy, C., Johnson, B. D., Ting, Y.-S., Bonaca, A., Dotter, A., & Speagle, J. S. 2020, *ApJ*, 900, 28
- Carollo, D., Chiba, M., Ishigaki, M., Freeman, K., Beers, T. C., Lee, Y. S., Tissera, P., Battistini, C., & Primas, F. 2019, *ApJ*, 887, 22
- Carter, C., Conroy, C., Zaritsky, D., Ting, Y.-S., Bonaca, A., Naidu, R. P., Johnson, B. D., Cargile, P. A., Caldwell, N., Speagle, J., & Han, J. J. 2021, *ApJ*, 908, 208
- Cayrel, R., Depagne, E., Spite, M., Hill, V., Spite, F., François, P., Plez, B., Beers, T., Primas, F., Andersen, J., Barbuy, B., Bonifacio, P., Molaro, P., & Nordström, B. 2004, *A&A*, 416, 1117
- Chaplin, W. J., Serenelli, A. M., Miglio, A., et al. 2020, *Nature Astronomy*, 4, 382
- Chen, B., Ting, Y.-S., & Hayden, M. 2023, arXiv e-prints, arXiv:2308.15976
- Chiappini, C., Matteucci, F., & Gratton, R. 1997, *ApJ*, 477, 765
- Chiba, M. & Beers, T. C. 2000, *The Astronomical Journal*, 119, 2843
- Choi, J., Dotter, A., Conroy, C., et al. 2016, *ApJ*, 823, 102
- Conroy, C., Bonaca, A., Cargile, P., et al. 2019, *ApJ*, 883, 107
- Das, P., Hawkins, K., & Jofré, P. 2020, *MNRAS*, 493, 5195
- Di Matteo, P., Haywood, M., Lehnert, M. D., Katz, D., Khoperskov, S., Snaith, O. N., Gómez, A., & Robichon, N. 2019, *A&A*, 632, A4
- Dotter, A., Conroy, C., Cargile, P., & Asplund, M. 2017, *ApJ*, 840, 99
- Edvardsson, B., Andersen, J., Gustafsson, B., Lambert, D. L., Nissen, P. E., & Tomkin, J. 1993, *A&A*, 275, 101
- Fabricant, D., Fata, R., Roll, J., et al. 2005, *PASP*, 117, 1411
- Fakhouri, O., Ma, C.-P., & Boylan-Kolchin, M. 2010, *MNRAS*, 406, 2267
- Few, C. G., Courty, S., Gibson, B. K., Michel-Dansac, L., & Calura, F. 2014, *MNRAS*, 444, 3845
- Gaia Collaboration, Brown, A. G. A., Vallenari, A., et al. 2021, *A&A*, 649, A1
- Gallart, C., Bernard, E. J., Brook, C. B., Ruiz-Lara, T., Cassisi, S., Hill, V., & Monelli, M. 2019, *Nature Astronomy*, 3, 932
- Gilmore, G. & Reid, N. 1983, *MNRAS*, 202, 1025
- Grand, R. J. J., Bustamante, S., Gómez, F. A., et al. 2018a, *MNRAS*, 474, 3629
- Grand, R. J. J., Gómez, F. A., Marinacci, F., Pakmor, R., Springel, V., Campbell, D. J. R., Frenk, C. S., Jenkins, A., & White, S. D. M. 2017, *MNRAS*, 467, 179
- Grand, R. J. J., Helly, J., Fattahi, A., et al. 2018b, *MNRAS*, 481, 1726
- Gratton, R. G., Carretta, E., Claudi, R., Lucatello, S., & Barbieri, M. 2003, *A&A*, 404, 187

- Griffith, E. J., Sukhbold, T., Weinberg, D. H., Johnson, J. A., Johnson, J. W., & Vincenzo, F. 2021, *ApJ*, 921, 73
- Guedes, J., Callegari, S., Madau, P., & Mayer, L. 2011, *ApJ*, 742, 76
- Gurvich, A. B., Stern, J., Faucher-Giguère, C.-A., Hopkins, P. F., Wetzel, A., Moreno, J., Hayward, C. C., Richings, A. J., & Hafen, Z. 2022, arXiv e-prints, arXiv:2203.04321
- Hafen, Z., Stern, J., Bullock, J., et al. 2022, arXiv e-prints, arXiv:2201.07235
- Han, D. R., Lee, Y. S., Kim, Y. K., & Beers, T. C. 2020, *ApJ*, 896, 14
- Harris, C. R., Millman, K. J., van der Walt, S. J., et al. 2020, *Nature*, 585, 357
- Hasselquist, S., Hayes, C. R., Lian, J., et al. 2021, *ApJ*, 923, 172
- Hawkins, K., Jofré, P., Masseron, T., & Gilmore, G. 2015, *MNRAS*, 453, 758
- Hayden, M. R., Bovy, J., Holtzman, J. A., et al. 2015, *ApJ*, 808, 132
- Haywood, M., Di Matteo, P., Lehnert, M. D., Katz, D., & Gómez, A. 2013, *A&A*, 560, A109
- Haywood, M., Di Matteo, P., Lehnert, M. D., Snaith, O., Khoperskov, S., & Gómez, A. 2018, *ApJ*, 863, 113
- Heger, A. & Woosley, S. E. 2010, *ApJ*, 724, 341
- Helmi, A., Babusiaux, C., Koppelman, H. H., Massari, D., Veljanoski, J., & Brown, A. G. A. 2018, *Nature*, 563, 85
- Hendricks, B., Koch, A., Lanfranchi, G. A., Boeche, C., Walker, M., Johnson, C. I., Peñarrubia, J., & Gilmore, G. 2014, *ApJ*, 785, 102
- Horta, D., Schiavon, R. P., Mackereth, J. T., et al. 2021, *MNRAS*, 500, 1385
- Ibata, R. A., Lewis, G. F., Irwin, M. J., & Quinn, T. 2002, *MNRAS*, 332, 915
- Johnson, B. D., Conroy, C., Naidu, R. P., Bonaca, A., Zaritsky, D., Ting, Y.-S., Cargile, P. A., Han, J. J., & Speagle, J. S. 2020, *ApJ*, 900, 103
- Johnson, J. W., Weinberg, D. H., Vincenzo, F., Bird, J. C., Loebman, S. R., Brooks, A. M., Quinn, T. R., Christensen, C. R., & Griffith, E. J. 2021, *MNRAS*, 508, 4484
- Johnston, K. V., Spergel, D. N., & Haydn, C. 2002, *ApJ*, 570, 656
- Kobayashi, C., Karakas, A. I., & Lugaro, M. 2020, *ApJ*, 900, 179
- Koppelman, H., Helmi, A., & Veljanoski, J. 2018, *ApJL*, 860, L11
- Krujijssen, J. M. D., Pfeffer, J. L., Reina-Campos, M., Crain, R. A., & Bastian, N. 2019, *MNRAS*, 486, 3180
- Lee, Y. S., Beers, T. C., An, D., et al. 2011, *ApJ*, 738, 187
- Leroy, A. K., Walter, F., Brinks, E., Bigiel, F., de Blok, W. J. G., Madore, B., & Thornley, M. D. 2008, *AJ*, 136, 2782
- Leung, H. W. & Bovy, J. 2019, *MNRAS*, 489, 2079
- Loebman, S. R., Debattista, V. P., Nidever, D. L., Hayden, M. R., Holtzman, J. A., Clarke, A. J., Roškar, R., & Valluri, M. 2016, *ApJL*, 818, L6
- Loebman, S. R., Roškar, R., Debattista, V. P., Ivezić, Ž., Quinn, T. R., & Wadsley, J. 2011, *ApJ*, 737, 8
- Mackereth, J. T., Crain, R. A., Schiavon, R. P., Schaye, J., Theuns, T., & Schaller, M. 2018, *MNRAS*, 477, 5072
- Majewski, S. R., Schiavon, R. P., Frinchaboy, P. M., et al. 2017, *AJ*, 154, 94
- Maoz, D. & Graur, O. 2017, *ApJ*, 848, 25
- Mason, A. C., Crain, R. A., Schiavon, R. P., Weinberg, D. H., Pfeffer, J., Schaye, J., Schaller, M., & Theuns, T. 2024, *MNRAS*
- Massari, D., Koppelman, H. H., & Helmi, A. 2019, *A&A*, 630, L4
- Micalì, A., Matteucci, F., & Romano, D. 2013, *MNRAS*, 436, 1648
- Minchev, I., Chiappini, C., & Martig, M. 2013, *A&A*, 558, A9
- Minchev, I., Martig, M., Streich, D., Scannapieco, C., de Jong, R. S., & Steinmetz, M. 2015, *ApJL*, 804, L9
- Montalbán, J., Mackereth, J. T., Miglio, A., et al. 2021, *Nature Astronomy*, 5, 640
- Morrison, H. L., Flynn, C., & Freeman, K. C. 1990, *AJ*, 100, 1191
- Myeong, G. C., Vasiliev, E., Iorio, G., Evans, N. W., & Belokurov, V. 2019, *MNRAS*, 488, 1235
- Naidu, R. P., Conroy, C., Bonaca, A., Johnson, B. D., Ting, Y.-S., Caldwell, N., Zaritsky, D., & Cargile, P. A. 2020, *ApJ*, 901, 48
- Naidu, R. P., Conroy, C., Bonaca, A., Zaritsky, D., Weinberger, R., Ting, Y.-S., Caldwell, N., Tacchella, S., Han, J. J., Speagle, J. S., & Cargile, P. A. 2021, *ApJ*, 923, 92
- Naidu, R. P., Ji, A. P., Conroy, C., et al. 2022, *ApJL*, 926, L36
- Nidever, D. L., Bovy, J., Bird, J. C., et al. 2014, *ApJ*, 796, 38
- Nidever, D. L., Hasselquist, S., Hayes, C. R., et al. 2020, *ApJ*, 895, 88
- Nissen, P. E. & Schuster, W. J. 2010, *A&A*, 511, L10
- Norris, J., Bessell, M. S., & Pickles, A. J. 1985, *ApJS*, 58, 463
- Pontzen, A., Roškar, R., Stinson, G. S., Woods, R., Reed, D. M., Coles, J., & Quinn, T. R. 2013, pynbody: Astrophysics Simulation Analysis for Python, astrophysics Source Code Library, ascl:1305.002
- Pontzen, A. & Tremmel, M. 2018, *The Astrophysical Journal Supplement Series*, 237, 23
- Price-Whelan, A., Sipocz, B., Major, S., & Oh, S. 2017, *adrm/gala: v0.2.1*
- Price-Whelan, A. M. 2017, *The Journal of Open Source Software*, 2
- Re Fiorentin, P., Lattanzi, M. G., & Spagna, A. 2019, *MNRAS*, 484, L69
- Reddy, B. E., Lambert, D. L., & Allende Prieto, C. 2006, *MNRAS*, 367, 1329
- Renaud, F., Agertz, O., Read, J. I., Ryde, N., Andersson, E. P., Bensby, T., Rey, M. P., & Feuillet, D. K. 2021, *MNRAS*, 503, 5846
- Rix, H.-W. & Bovy, J. 2013, *A&A Rev.*, 21, 61
- Ruchti, G. R., Fulbright, J. P., Wyse, R. F. G., et al. 2011, *ApJ*, 737, 9
- Rybizki, J., Demleitner, M., Fouesneau, M., Bailer-Jones, C., Rix, H.-W., & Andrae, R. 2018, *PASP*, 130, 074101
- Schönrich, R. & Binney, J. 2009, *MNRAS*, 399, 1145
- Sestito, F., Martin, N. F., Starkenburg, E., et al. 2020, *MNRAS*, 497, L7
- Sharma, S., Hayden, M. R., & Bland-Hawthorn, J. 2021, *MNRAS*, 507, 5882
- Snaith, O., Haywood, M., Di Matteo, P., Lehnert, M., Katz, D., & Khoperskov, S. 2022, *A&A*, 659, A64
- Spitoni, E., Silva Aguirre, V., Matteucci, F., Calura, F., & Grisoni, V. 2019, *A&A*, 623, A60
- Stern, J., Faucher-Giguère, C.-A., et al. 2021, *ApJ*, 911, 88
- Szentgyorgyi, A., Furesz, G., Cheimets, P., et al. 2011, *PASP*, 123, 1188
- Villalobos, Á. & Helmi, A. 2008, *MNRAS*, 391, 1806
- Vincenzo, F., Matteucci, F., Belfiore, F., & Maiolino, R. 2016, *MNRAS*, 455, 4183
- Vincenzo, F., Spitoni, E., Calura, F., Matteucci, F., Silva Aguirre, V., Miglio, A., & Cescutti, G. 2019, *MNRAS*, 487, L47
- Wang, L., Dutton, A. A., Stinson, G. S., Macciò, A. V., Penzo, C., Kang, X., Keller, B. W., & Wadsley, J. 2015, *MNRAS*, 454, 83
- Weinberg, D. H., Andrews, B. H., & Freudenburg, J. 2017, *ApJ*, 837, 183
- Wetzel, A., Hayward, C. C., Sanderson, R. E., et al. 2022, arXiv e-prints, arXiv:2202.06969
- Wetzel, A. R., Hopkins, P. F., Kim, J.-h., Faucher-Giguère, C.-A., Kereš, D., & Quataert, E. 2016, *ApJL*, 827, L23
- Williams, C. C., Curtis-Lake, E., Hainline, K. N., et al. 2018, *ApJS*, 236, 33
- Xiang, M. & Rix, H.-W. 2022, arXiv e-prints, arXiv:2203.12110
- Yu, S., Bullock, J. S., Klein, C., et al. 2021, *MNRAS*, 505, 889
- Zolotov, A., Willman, B., Brooks, A. M., et al. 2009, *ApJ*, 702, 1058

APPENDIX

A. COMPARISON TO APOGEE

In this Appendix we compare the H3 chemistry of in-situ (prograde) stars to stars in APOGEE DR17 (Abdurro'uf et al. 2021). For distances and angular momenta we use the AstroNN value-added catalog from Leung & Bovy (2019). Following Belokurov & Kravtsov (2022), we restrict the APOGEE catalog to $\log g < 3.0$ and remove stars associated with the Magellanic Cloud program and any cluster-related program. We also remove stars with potentially problematic measurements via the flags STAR_BAD, TEFF_BAD, LOGG_BAD, PERSIST_HIGH, VERY_BRIGHT_NEIGHBOR, PERSIST_JUMP_POS, PERSIST_JUMP_NEG, or SUSPECT_RV_COMBINATION.

We also require $\text{SNR} > 200$, *Gaia* EDR3 parallax $\text{SNR} > 10$, and agreement between the *Gaia* parallax and the AstroNN distances to 50%. To enable a fair comparison to the H3 sample we restrict the APOGEE sample to $6 < R_{\text{gal}} < 10$ kpc. Finally, to focus on the in-situ (prograde) population we select stars with $L_Z < -500 \text{ km s}^{-1} \text{ kpc}^{-1}$ (the AstroNN coordinate system has a different sign than ours; we have converted their system to ours for consistency). With these cuts the final sample contains 74,806 stars. For this sample the median formal uncertainty on [Mg/Fe] and [Fe/H] are ≈ 0.01 .

Figure A1 compares the chemistry of prograde APOGEE and H3 stars. For the former we use [Mg/Fe] since the H3 spectral window is mostly sensitive to Mg among the α elements. APOGEE does not take atomic diffusion into account, and so in this figure we use the surface abundances

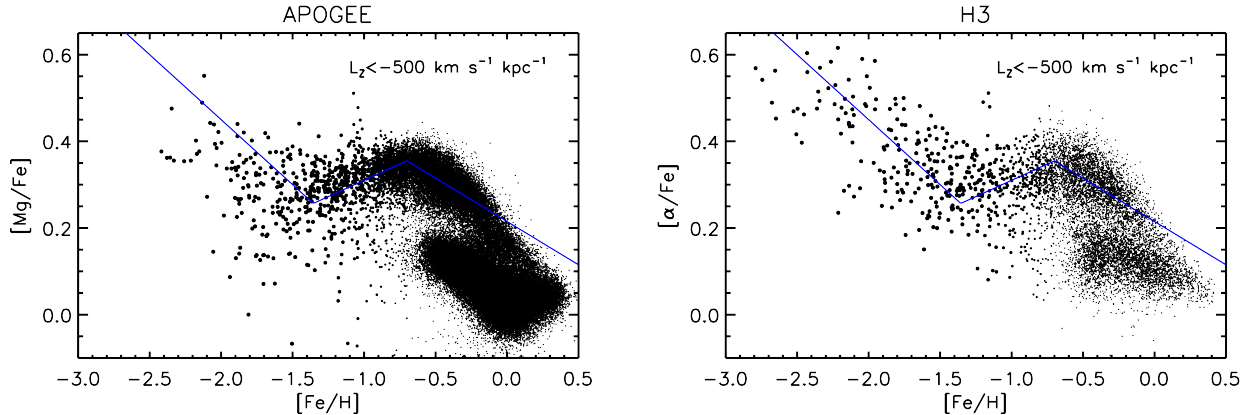


Figure A1. Comparison between APOGEE (left panel) and H3 (right panel) data for prograde stars ($L_z < -500 \text{ km s}^{-1} \text{ kpc}^{-1}$). The blue line is intended to guide the eye. The overall trend of the high- α sequence is the same in the two surveys, although the APOGEE data are offset to lower $[\text{Mg}/\text{Fe}]$ at $[\text{Fe}/\text{H}] \lesssim -1.5$. In H3 only the global $[\alpha/\text{Fe}]$ is measured, although it is primarily sensitive to Mg. Therefore, in the comparison to APOGEE we plot $[\text{Mg}/\text{Fe}]$ for that survey. In both panels the symbol size is inversely proportional to metallicity in order to draw attention to the low-metallicity sequence.

reported for H3 stars, as opposed to the initial composition. The behavior of the high- α sequences are nearly identical for $[\text{Fe}/\text{H}] \gtrsim -1.3$. This agreement provides confirmation that both abundance scales are reliable, as the analysis pipelines of H3 and APOGEE are quite different (although with common elements such as the assumption of LTE). At lower metallicities the APOGEE data shows an increase in $[\text{Mg}/\text{Fe}]$ as also seen in the H3 data. However, the normalization is lower by ≈ 0.1 , or, alternatively, the metallicity scale of APOGEE and H3 are offset by ≈ 0.1 at $[\text{Fe}/\text{H}] \lesssim -1.5$ (see Cargile et al. 2020). Overall, this comparison provides independent confirmation of the abundance trends reported in this paper.

B. ON THE USE OF CHEMISTRY TO IDENTIFY ACCRETED STARS

Hawkins et al. (2015) proposed the use of the abundance ratios $[\text{Al}/\text{Fe}]$ and $[\text{Mg}/\text{Mn}]$ to separate accreted and in-situ stars. A number of authors have since used some combination of these abundance ratios (and $[\text{Fe}/\text{H}]$) to separate accreted from in-situ stars (e.g., Das et al. 2020; Horta et al. 2021; Belokurov & Kravtsov 2022). In this section we briefly revisit these selections in the context of metal-poor in-situ stars.

Figure B1 shows two projections of abundance space: $[\text{Al}/\text{Fe}]$ vs. $[\text{Fe}/\text{H}]$ (left panel) and $[\text{Mg}/\text{Mn}]$ vs. $[\text{Al}/\text{Fe}]$ (right panel). The boxes mark regions where accreted stars are supposed to reside (cf. Das et al. 2020; Horta et al. 2021; Belokurov & Kravtsov 2022). However, in this figure we plot

only APOGEE stars with significant prograde motion, specifically $L_z < -10^3 \text{ km s}^{-1} \text{ kpc}^{-1}$. Such stars have an average eccentricity of 0.15 – i.e., they are on nearly circular orbits and so are very unlikely to be accreted stars. In the left panel one sees that nearly every prograde star at $[\text{Fe}/\text{H}] < -1.5$ resides in the accretion selection box. In the right panel stars with $[\text{Fe}/\text{H}] < -1.2$ are displayed as large symbols; one clearly sees that the overwhelming majority of such stars reside in the accretion selection box. The contamination of in-situ stars in the accretion selection box at low metallicity was also pointed out by Horta et al. (2021) and Belokurov & Kravtsov (2022).

Figure B1 shows that the use of these chemistry-based selections will incorrectly assign genuine low-metallicity, in-situ stars to the accreted population. The contamination of the resulting accretion-selected stars is likely to be low, as low-metallicity in-situ stars are rare. However, the selection will bias (truncate) the low-metallicity in-situ population. We therefore urge caution when using a chemistry-based separation between in-situ and accreted stars if one is interested in low-metallicity in-situ stars.

This paper was built using the Open Journal of Astrophysics \LaTeX template. The OJA is a journal which provides fast and easy peer review for new papers in the astro-ph section of the arXiv, making the reviewing process simpler for authors and referees alike. Learn more at <http://astro.theoj.org>.

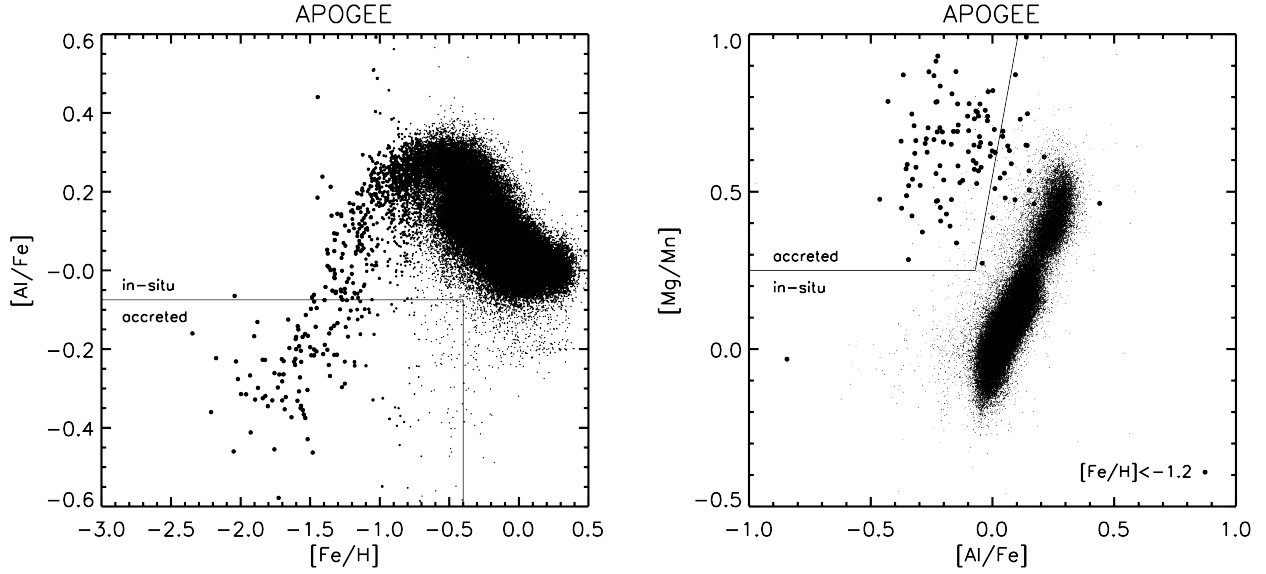


Figure B1. Chemistry of stars in APOGEE with $L_Z < -10^3 \text{ km s}^{-1} \text{ kpc}^{-1}$. Such stars have a median eccentricity of $e \approx 0.2$, i.e., they are on nearly circular prograde orbits and so are very unlikely to be accreted. Left panel: $[\text{Al}/\text{Fe}]$ vs. $[\text{Fe}/\text{H}]$. This diagram was recently used by Belokurov & Kravtsov (2022) to separate accreted and in-situ stars, with the former presumed to occupy the lower left region indicated by the box. In this same region we also clearly see metal-poor in-situ stars. Symbol size is inversely proportional to metallicity in order to draw attention to the low-metallicity sequence. Right panel: $[\text{Mg}/\text{Mn}]$ vs. $[\text{Al}/\text{Fe}]$. This diagram has been proposed as an efficient way to separate accreted and in-situ stars, with the former occupying the upper left region indicated by the lines (see e.g., Hawkins et al. 2015; Horta et al. 2021). In this panel stars with $[\text{Fe}/\text{H}] < -1.2$ are indicated with large symbols. It is clear that the in-situ, metal-poor stars have similar chemical make-up as accreted stars, at least with regards to $[\text{Al}/\text{Fe}]$ and $[\text{Mg}/\text{Mn}]$. This method of selecting accreted stars should therefore be treated with caution at low metallicity.